

Symmetric and antisymmetric components of polar-amplified warming

SPENCER A. HILL *

Lamont-Doherty Earth Observatory, Columbia University, Palisades, New York

NATALIE J. BURLS

Center for Ocean-Land-Atmosphere Studies, Department of Atmospheric, Oceanic, and Earth Sciences, George Mason University, Fairfax, Virginia

ALEXEY FEDOROV

Department of Earth & Planetary Sciences, Yale University, New Haven, Connecticut

TIMOTHY M. MERLIS

Department of Atmospheric and Oceanic Sciences, McGill University, Montreal, Quebec, Canada

ABSTRACT

CO₂-forced surface warming simulated by general circulation models (GCMs) is initially rapid in the Arctic but sluggish over Antarctica and the Southern Ocean—a primarily hemispherically antisymmetric signal. Nevertheless, we show the following robust behaviors of the global-mean-normalized, hemispherically symmetric warming pattern in fourteen GCMs from the LongRunMIP repository: to leading order, the pattern established in the first decade persists over subsequent millennia, and to next order it becomes moderately more polar-amplified with time. Conversely, the antisymmetric component gradually weakens. These behaviors also emerge in 3,000-year simulations with the CESM1.0.4 GCM under instantaneous 2 to 16×CO₂ increases or with perturbed cloud albedo fields yielding a more polar-amplified, early Pliocene-like climate. Simulations in a diffusive moist energy balance model (MEBM) with the radiative feedback parameter (λ) and ocean heat uptake (\mathcal{O}) diagnosed from the CESM 4×CO₂ simulation at different timescales adequately reproduce the GCM warming. The symmetric, mean-normalized warming pattern is weakly modified even in MEBM simulations with the antisymmetric components of λ and \mathcal{O} artificially enhanced. The persistence of the symmetric warming signal therefore must be driven by the symmetric components of λ and \mathcal{O} , and we argue that they induce canceling processes, some of which act to enhance, and others to weaken, polar amplification with time. We further distill the GCM behaviors in terms of Arctic and Antarctic amplification indices using a three-box, two-timescale model.

1. Introduction

Climatological surface temperatures decrease from the equator toward either pole, a hemispherically symmetric signature much larger than the antisymmetric deviations therefrom. Fig. 1(a) illustrates this via zonal-mean, annual-mean surface temperatures from a preindustrial control simulation in the Community Earth System Model version 1.0.4 (henceforth CESM) general circulation model (GCM) whose formulation will be described below. Evidently, the symmetric annual-mean forcing of insolation and approximately uniform (though not exactly, c.f. Merlis 2015; Huang et al. 2017) forcing of CO₂ and other well-mixed greenhouse gases outweigh the antisym-

metric components of Earth’s ocean basins, orography, sea ice, and atmospheric and oceanic circulations.

Anomalous surface temperatures forced by CO₂ perturbations increase in magnitude from the equator toward either pole at equilibrium, but this polar amplification includes antisymmetric signatures at multiple timescales. Fig. 1(b) illustrates this via anomalous surface temperatures in a standard abrupt 4×CO₂ simulation in the same GCM averaged over four time periods (years 1-10, 21-100, 701-800, and 2901-3000). In the first decades after CO₂ is increased, prevailing upwelling in the Southern Ocean (e.g. Armour et al. 2013; Marshall et al. 2015) impedes warming in the southern high latitudes (likely reinforced by resulting changes in the local lapse rate and cloud fields; Senior and Mitchell 2000; Rugenstein et al. 2020), while weakly negative (or even slightly positive) radiative feedbacks in northern high latitudes (e.g. Stuecker et al.

*Corresponding author address: Spencer Hill, 207B Oceanography, Lamont-Doherty Earth Observatory, 61 Route 9W, Palisades, NY 10964
E-mail: shill@ldeo.columbia.edu

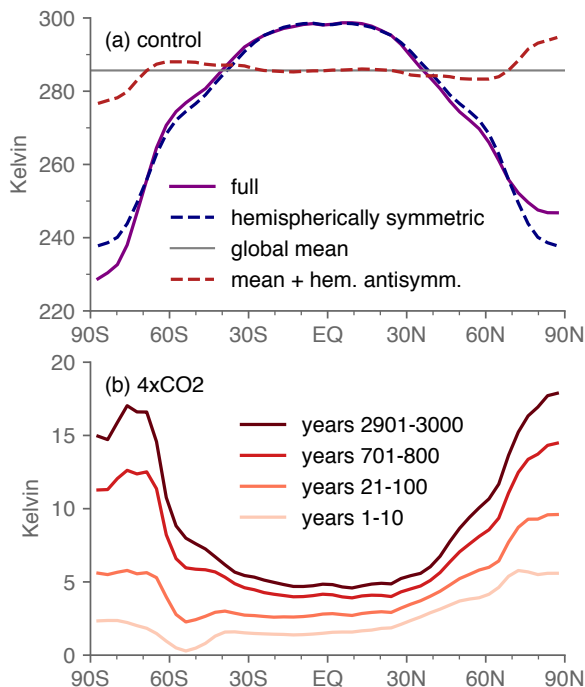


FIG. 1. (a) Climatological annual-mean, zonal-mean surface air temperature in the preindustrial control simulation, the hemispherically symmetric component thereof, the global mean thereof, and the global mean plus the hemispherically antisymmetric component, as indicated in the legend. The simulation was performed in a low-resolution configuration of the CESM version 1.0.4 climate model, with results averaged over years 701–800. (b) Anomalous zonal-mean surface air temperature in the abrupt $4\times\text{CO}_2$ simulation, averaged over four time periods as indicated in the legend. Both panels have units Kelvin.

2018) among several other processes (Feldl et al. 2017; Russotto and Biasutti 2020; Henry et al. 2021) promote Arctic warming. The Antarctic tends to partially catch up over subsequent decades in roughly century-length simulations in CMIP5 (Andrews et al. 2015) and CMIP6 (Dong et al. 2020) GCMs and millennial. Held et al. (2010) diagnose two, well-separated timescales of CO_2 -induced warming in a multi-century GCM simulation, one fast (a few years) and appreciably antisymmetric, the other slow (decades to centuries) and largely symmetric (see also Geoffroy and Saint-Martin 2014).

In longer, millennial-scale integrations, changes in deep-ocean circulation become relevant (and can be non-monotonic, c.f. Jansen et al. 2018), perturbing the prevailing antisymmetric transport of heat from the southern to the northern hemisphere by the Atlantic Meridional Overturning Circulation. For example, in a 3,000-year GCM simulation with perturbed cloud albedos yielding a surface climate resembling the early Pliocene (~ 4 Ma), a Pacific Meridional Overturning Circulation emerges after $\sim 1,500$ years, increasing the heat convergence into

the northern hemisphere (Burls et al. 2017). Nevertheless, in multi-millennial GCM integrations run to near-equilibrium (e.g. Danabasoglu and Gent 2009; Li et al. 2013; Rugenstein et al. 2019) and integrations to equilibrium of slab-ocean GCMs (e.g. Armour et al. 2013) and simple diffusive moist energy balance models (MEBMs) (e.g. Merlis and Henry 2018; Armour et al. 2019), both polar caps ultimately warm much more than the Tropics—a primarily symmetric signal.

Here, we demonstrate in fourteen GCMs from the LongRunMIP repository (Rugenstein et al. 2019), 3,000-year simulations in CESM, and an MEBM that the hemispherically symmetric component of zonal-mean warming that emerges in the first decade after abrupt CO_2 forcing—though unique to each model—to leading order stays fixed all the way to equilibrium when normalized by the contemporaneous global-mean surface warming and varies weakly with the forcing magnitude. In a majority of models, to next order the symmetric pattern becomes modestly more polar-amplified with time. This implies that a single decade of simulation yields a fairly accurate approximation to the symmetric, mean-normalized warming signal at equilibrium. Combined with a reasonable estimate for the equilibrium climate sensitivity (i.e. the global-mean warming at equilibrium), it would yield the non-normalized symmetric warming pattern at equilibrium—which to first order captures the full zonal-mean pattern since the antisymmetric warming component tends to be weak at equilibrium.

Some collapse of zonal-mean surface air temperature responses under CO_2 at different timescales when mean-normalized can be inferred in the existing literature—across timescales in one GCM (c.f. Fig. 4a of Armour et al. 2013) and across GCMs at individual timescales (c.f. Fig. 6 of Rugenstein et al. 2019). And a strong similarity between the spatial patterns of the sea surface temperature (SST) response in the Indo-Pacific ocean in experiments with different CO_2 forcings has been noted, but not fully explained, by Heede et al. (2020). In terms of bulk Northern vs. Southern Hemisphere averages, observations and GCMs exhibit considerable symmetry in top-of-atmosphere (TOA) albedo, both climatologically (Voigt et al. 2013; Stephens et al. 2015) and, for GCMs, under hemispherically antisymmetric external forcing (Voigt et al. 2014). Previdi et al. (2020) argue that Arctic amplification emerges on a sub-annual timescale after imposed CO_2 forcing.

After describing our methods in Section 2, we argue that:

- in millennial-length, CO_2 -forced simulations in fourteen GCMs analyzed from the LongRunMIP repository, the mean-normalized, symmetric surface warming patterns respond robustly, changing weakly to

leading order and becoming slightly more polar-amplified to next order in most models (Section 3);

- the same holds in CESM both under $2\text{--}16\times\text{CO}_2$ and in the aforementioned Pliocene-like, perturbed-albedo simulation, though with forcing-dependent patterns, as does a pronounced weakening of the antisymmetric component (Section 4);
- an MEBM can emulate the CESM $4\times\text{CO}_2$ responses at different timescales given the appropriate CESM fields as inputs, and this holds even if the antisymmetric components of the radiative feedback parameter and ocean heat uptake fields are strongly, artificially enhanced (Section 5);
- and, at the level of bulk Arctic and Antarctic amplification indices, a simple three-box, two-timescale model of the Arctic, Antarctic, and lower-latitude regions reasonably captures the time evolution of the symmetric and antisymmetric components (Section 6).

We then conclude with summary and discussion (Section 7).

2. Methods

a. Calculation procedures

We decompose fields into components that are symmetric and antisymmetric about the equator. Symbolically for a given field χ ,

$$\chi(\varphi) = \chi_{\text{sym}}(\varphi) + \chi_{\text{asym}}(\varphi),$$

where φ is latitude,

$$\chi_{\text{sym}} \equiv \frac{\chi(\varphi) + \chi(-\varphi)}{2}$$

is the symmetric component, and

$$\chi_{\text{asym}} \equiv \frac{\chi(\varphi) - \chi(-\varphi)}{2}$$

is the antisymmetric component. The symmetric component is an even function of latitude whose global-mean value (which we denote by overbars) is identical to the full field's global mean [$\chi_{\text{sym}}(\varphi) = \chi_{\text{sym}}(-\varphi)$ and $\overline{\chi_{\text{sym}}} = \overline{\chi}$], and the antisymmetric component is an odd function of latitude whose global mean is zero [$\chi_{\text{asym}}(\varphi) = -\chi_{\text{asym}}(-\varphi)$ and $\overline{\chi_{\text{asym}}} = 0$].

Following convention, we define Arctic amplification as the ratio of annual-mean surface air temperature change averaged over $60\text{--}90^\circ\text{N}$ to the global-mean surface air temperature change, Antarctic amplification analogously but using $60\text{--}90^\circ\text{S}$, and global polar amplification as the average of the Arctic and Antarctic amplification values.

We focus on temporal averages over four time periods (similar to those of Armour et al. 2013): years 1–10 and 21–100 (during which both the atmosphere and ocean are rapidly responding), 701–800 (during which the atmosphere is in a nearly statistically steady state but the ocean remains slowly varying), and 2901–3000 (at which time the deep ocean has nearly equilibrated).

b. LongRunMIP

LongRunMIP (Rugenstein et al. 2019) comprises increased- CO_2 simulations from sixteen CMIP5-class GCMs that span from nearly one thousand to several thousand years, and we analyze the fourteen listed in Table 1. This includes all but one of the fifteen models for which output was available regridded to a common $2.5\times 2.5^\circ$ grid (c.f. Table 2 of Rugenstein et al. 2019), with CESM104 omitted to avoid duplication because it is effectively the same model described below that we analyze separately. All participating models performed abrupt $4\times\text{CO}_2$ simulations, and a subset contributed additional perturbed- CO_2 simulations. For most models the abrupt $4\times\text{CO}_2$ simulation is 1000 years or longer, but in a few models it is much shorter while another increased- CO_2 simulation is millennial. We handle those models as follows. For the transient periods of years 1–10 and 21–100, we use the abrupt CO_2 quadrupling simulation (“abrupt4x”) for all models. For the 701–800 period, we use the RCP8.5 simulation in ECEARTH, 1% to quadrupling simulation in ECHAM5MPIOM and MIROC32, and 1% to doubling in GFDLCM3 and GFDLESM2M. The mean-normalized warming patterns are similar enough across the different experimental protocols for each model to justify this mix-and-match approach (not shown). With these choices, all models have data extending through the 701–800 period, and ECHAM5MPIOM, FAMOUS, MPIESM11, GFDLCM3, GFDLESM2M, and GISSE2R all have data for the 2901–3000 period also.

Different LongRunMIP models exhibit different levels of drift in their control simulations, which we account for as follows. For each of the four time periods, we compute the difference between the perturbation simulation and the control at that time period if the control simulation extends that long. For periods after the end of the control simulation, we subtract from the perturbation simulation an average over the entire duration of the control simulation, except for GFDLCM3: it warms by nearly a degree over the first two millennia, so we average over the subsequent 2,500 years.

c. CESM perturbed- CO_2 and Pliocene-like simulations

In addition to LongRunMIP, we use the National Center for Atmospheric Research (NCAR) Community Earth System Model version 1.0.4 (henceforth CESM), in its

Model	Control duration	701-800 sim.	2901-3000 sim.	symm. RMSE	asymm. RMSE
CCSM3	1530	4×CO ₂	none	0.20	0.25
CNRMCM61	2000	4×CO ₂	none	0.13	0.26
ECEARTH	508	RCP8.5	RCP8.5	0.06	0.26
ECHAM5MPIOM	100	4×CO ₂	1%4×CO ₂	0.11	0.41
FAMOUS	3000	4×CO ₂	4×CO ₂	0.09	0.22
GFDLCM3	5200	1%2×CO ₂	1%2×CO ₂	0.17	0.29
GFDLESM2M	1340	1%2×CO ₂	1%2×CO ₂	0.26	0.57
GISSE2R	5225	4×CO ₂	4×CO ₂	0.29	0.50
HadCM3L	1000	4×CO ₂	none	0.06	0.17
HadGEM2	239	4×CO ₂	none	0.09	0.17
IPSLCM5A	1000	4×CO ₂	none	0.13	0.19
MIROC32	680	1%2×CO ₂	none	0.05	0.19
MPIESM11	2000	4×CO ₂	4×CO ₂	0.23	0.28
MPIESM12	1237	4×CO ₂	none	0.19	0.23

TABLE 1. Details of the LongRunMIP models and simulations used. Columns, from left to right: Model name following Rugenstein et al. (2019) conventions; control simulation duration in years; simulation for which data over years 701-800 is taken; simulation for which data over years 2901-3000 is taken (or “none” if not available for any simulation in that model); root-mean-square error between the global-mean-normalized symmetric component of zonal-mean warming in the first decade vs. the last of the four averaging periods for which data exists; and same as the preceding column but for the antisymmetric rather than symmetric component.

low-resolution configuration (Shields et al. 2012). It consists of the Community Atmosphere Model, version 4 with its spectral dynamical core truncated at T31 resolution ($\sim 3.75^\circ \times 3.75^\circ$) and with 26 vertical levels coupled to the Parallel Ocean Program version 2 (POP2) with $\sim 3^\circ$ horizontal resolution and 60 vertical levels. We refer the interested reader to Shields et al. (2012) for additional details. The simulations analyzed are a standard preindustrial simulation, standard instantaneous CO₂ increase simulations of 2, 4, 8, and 16× preindustrial concentrations, and the Pliocene-like simulation mentioned in the Introduction (Burls and Fedorov 2014a). In the latter, atmospheric composition remains preindustrial, but—only in shortwave radiative transfer calculations—liquid water path is decreased by 240% poleward of 15° in both hemispheres, while both ice and liquid water paths are increased by 60% within 15°S – 15°N . This increases the albedo of the deep tropical band, promoting local cooling, but decreases the albedo elsewhere, promoting warming (Burls and Fedorov 2014b; Fedorov et al. 2015).

All five CESM1.0.4 simulations are run for 3,000 years. Model drift in the control simulation is modest relative to the forced temperature responses (not shown), and so for convenience we report anomalies in all periods in the perturbation experiments as differences with the control averaged over years 701-800.

d. Moist energy balance model

To gain more mechanistic understanding, we use a moist energy balance model (MEBM). MEBMs have been a useful simplified modeling framework to develop theory for the spatial pattern of warming in idealized contexts

(Flannery 1984; Rose et al. 2014; Roe et al. 2015; Merlis and Henry 2018; Russotto and Biasutti 2020) and to emulate the warming pattern in comprehensive GCMs (Hwang et al. 2011; Bonan et al. 2018). In short, the MEBM is forced with a realistic 4×CO₂ forcing and, for each of the four selected time periods, other input fields taken from the CESM 4×CO₂ simulation—either unmodified or perturbed as will be described in Section 5.

The MEBM’s governing equation is

$$\mathcal{C}\partial_t T(\varphi) = \mathcal{F}(\varphi) + \lambda(\varphi)T(\varphi) + \mathcal{O}(\varphi) + \mathcal{D}\nabla^2 h(\varphi), \quad (1)$$

where \mathcal{C} is the surface layer heat capacity, T is anomalous surface temperature, \mathcal{F} is the imposed radiative forcing, λ is the radiative feedback parameter, \mathcal{O} is the anomalous net surface flux (signed positive downward; also known as ocean heat uptake), \mathcal{D} is the diffusivity, and h is surface moist static energy (MSE). In words, the time tendency of the heat content of the surface layer (LHS) is determined by the combined effect of (RHS terms, left to right) the imposed radiative forcing, a radiative restoring term encompassing the net effect of all TOA radiative feedbacks and that varies linearly with the surface temperature anomaly, an imposed ocean heat uptake field, and the convergence of the anomalous column-integrated MSE flux, approximated as downgradient diffusion of surface MSE. The MEBM numerics and the calculations of each RHS term are conventional and detailed in the Appendix.

3. Results from LongRunMIP

Fig. 2 shows the mean-normalized, hemispherically symmetric surface air temperature anomaly in the perturbed-CO₂ simulations of the LongRunMIP models

as specified in the preceding section for each of the target time periods. Polar amplification is present in all models and time periods, though at any given time period the pattern differs substantially across models. But for each model the pattern emerging in the first decade changes weakly in later periods, with the following modest exceptions. In GISSE2R and GFDLESM2M, the pattern is similar for the first two periods but then changes nontrivially to a new one shared by the latter two periods. In CCSM3, MPIESM11, and MPIESM12, in the high latitudes only the pattern of the first decade is somewhat separated from subsequent periods. We have quantified how much the pattern changes in time for each model by computing the root-mean-square error of the pattern between the first decade and the last of the four analysis periods available for that model (either years 701–800 or 2901–3000). This value (printed in each panel and listed in Table 1) is lower for the symmetric component than for the antisymmetric component (discussed below) for every model.

To the extent that the pattern does change, it tends to become more polar-amplified with time. This holds unambiguously in nine of the fourteen models. Of the outliers, the pattern doesn't clearly change one way or another in HadCM3L and HadGEM2, becomes slightly less polar-amplified in FAMOUS and MIROC32, and is non-monotonic in time in ECEARTH.

Fig. 3 repeats Fig. 2 but shows the antisymmetric rather than symmetric component. All models exhibit greater initial warming in the Arctic compared to the Antarctic, and in all models this discrepancy weakens to some extent over subsequent decades to millennia. In most models, the changes in time in the antisymmetric component are considerably larger than those in the symmetric component, as quantified by the root mean square error metric described above (likewise printed in each panel and listed in Table 1). Nevertheless at equilibrium the extent of antisymmetry varies appreciably across models (e.g. weak for GISSE2R, appreciable for GFDLCM3).

From these results, we infer that the following responses to an abrupt CO_2 increase are robust—though not universal—across the GCMs analyzed and thus stand a good chance of being robust across other models. First, the mean-normalized symmetric warming pattern established in the first decade to leading order stays fixed all the way to (near) equilibrium. Second, to next order this pattern becomes moderately more polar-amplified in time. Third, the antisymmetric component weakens in magnitude with time. We now explore the forcing dependence of these behaviors using increased- CO_2 and Pliocene-like simulations in the CESM1.0.4 GCM, followed by an exploration of the underlying mechanism using the MEBM.

4. Results from $2\text{--}16\times\text{CO}_2$ and Pliocene simulations in CESM1.0.4

Fig. 4 shows the zonal-mean surface air temperature anomaly in CESM for each perturbed CO_2 simulation and time period. Surface warming occurs at all latitudes, is weakest and relatively flat at low latitudes, and increases nearly monotonically moving from low to high latitudes (peaking in the Southern Hemisphere from $\sim 65^\circ\text{S}$ for $2\times\text{CO}_2$ to $\sim 80^\circ\text{S}$ for $16\times\text{CO}_2$). Low-latitude warming ranges from ~ 2 to ~ 11 K, peak SH high-latitude warming from ~ 6 to ~ 25 K, and peak NH high-latitude warming (at the North Pole) from ~ 7 to ~ 34 K across the CO_2 simulations.

Fig. 5 shows maps of the mean-normalized surface air temperature response in each CO_2 simulation and for each time period, and Fig. 6(a) shows the zonal averages thereof. Enhanced warming at equilibrium in the southern high latitudes under $2\times\text{CO}_2$ is centered just off the Antarctic coast, primarily over the Weddell and Ross Seas. Nevertheless, the $2\times\text{CO}_2$ simulation is the only one in which southern hemisphere sea ice does not disappear entirely; under $16\times\text{CO}_2$ it is nearly gone by years 21–100, under $8\times\text{CO}_2$ by years 701–800, and under $4\times\text{CO}_2$ by years 2901–3000 (not shown). The zonal-mean patterns are quite similar across the simulations from the southern mid-latitudes to northern subtropics ($\sim 40^\circ\text{S}$ – 20°N) at all timescales and up to $\sim 50^\circ\text{S}$ and to the North Pole at subsequent timescales. At each timescale, the $2\times\text{CO}_2$ case is least like the others. The relative warming of the Arctic vs. Antarctic at (near) equilibrium varies roughly monotonically with the CO_2 value: under $2\times\text{CO}_2$ and $4\times\text{CO}_2$, the Arctic–Antarctic warming difference effectively vanishes by years 701–800 and reverses at equilibrium, while $4\times\text{CO}_2$ it stays near zero at equilibrium, and under 8 and $16\times\text{CO}_2$ it retains its original sign throughout.

Fig. 6(b) shows the hemispherically symmetric component of the mean-normalized surface warming patterns for each CO_2 value and averaging period. Apart from the first decade of the weakest perturbation, the mean-normalized symmetric components collapse tightly together, with warming less than the global-mean equatorward of $\sim 45^\circ\text{S/N}$ and greater than the global-mean poleward thereof. For all CO_2 values the signal becomes slightly more polar amplified in time, with low-latitude values decreasing and high-latitude values increasing. These behaviors are consistent with the LongRunMIP models. Across CO_2 concentrations, equilibrium polar amplification steadily decreases with CO_2 magnitude (except very near the poles).

Fig. 6(c) shows the hemispherically antisymmetric component of the mean-normalized surface warming patterns for each CO_2 value and averaging period. These vary appreciably across the four timescales, reflecting the gradual catching-up of Antarctic and Southern Ocean warm-

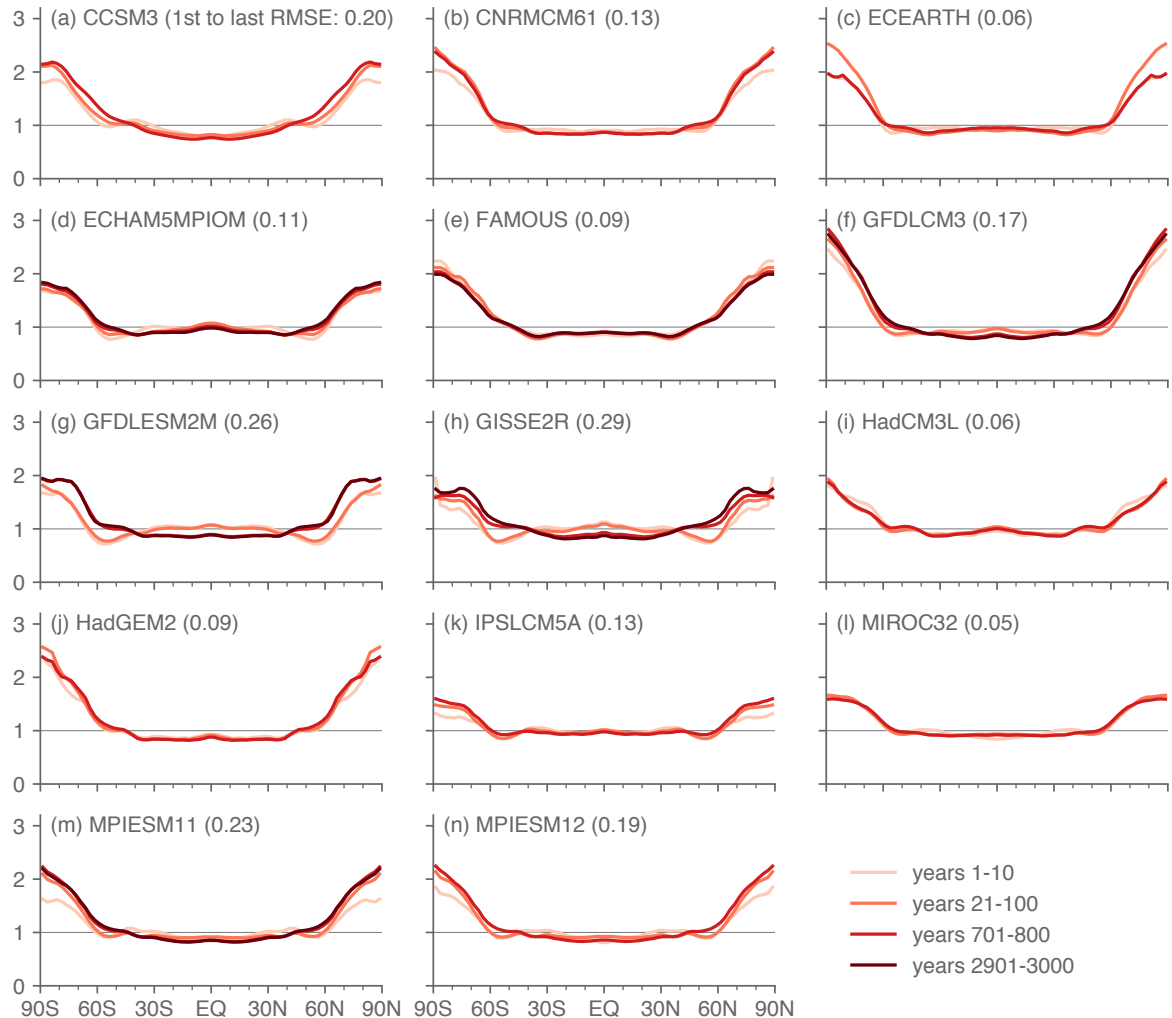


FIG. 2. For each of the fourteen models from LongRunMIP, global-mean-normalized, hemispherically symmetric component of zonal-mean surface air temperature change in the abrupt $4\times\text{CO}_2$ simulations in years 1–10 and 21–100 and either the abrupt $4\times\text{CO}_2$ or longer selected warming simulation as described in the text for years 701–800 and, if available, years 2901–3000, with each period as indicated in the legend in the lower right panel. Values in parentheses are the root-mean-square error between the patterns shown for the last available period (either 701–800 or 2901–3000) and the first decade.

ing with (and for 2 and $4\times\text{CO}_2$, surpassing) the initially rapid Arctic warming. Particularly in the initial century, the antisymmetric components group together more by timescale than by CO_2 value (in Fig. 6(c), compare curves with the same line markings to those with the same color). This would seem to reflect the timescales intrinsic to the physical processes underlying these responses—no matter how large a TOA forcing over the Southern Ocean, prevailing upwelling of water from depth inhibits initial local surface warming, while the deep ocean equilibration that acts to homogenize subsurface warming between the hemispheres take millennia.

Fig. 7 shows the zonal-mean surface air temperature anomalies in the Pliocene-like simulation in each of the

selected time periods, as the raw field and as the mean-normalized full, symmetric, and antisymmetric components. The corresponding fields already shown for the $2\text{--}16\times\text{CO}_2$ simulations are underlain for comparison. Because of the cooling effect of increased cloud albedo at lower latitudes, in the first decade the global-mean temperature response is weak, causing the mean-normalized field to separate from the other timescales. But the patterns over the subsequent three periods are very similar to one another. Like the CO_2 cases in CESM and the LongRunMIP models, they exhibit little change in time in the mean-normalized symmetric component (which is more polar-amplified than any of the CO_2 cases), but unlike the CO_2 simulations the antisymmetric component

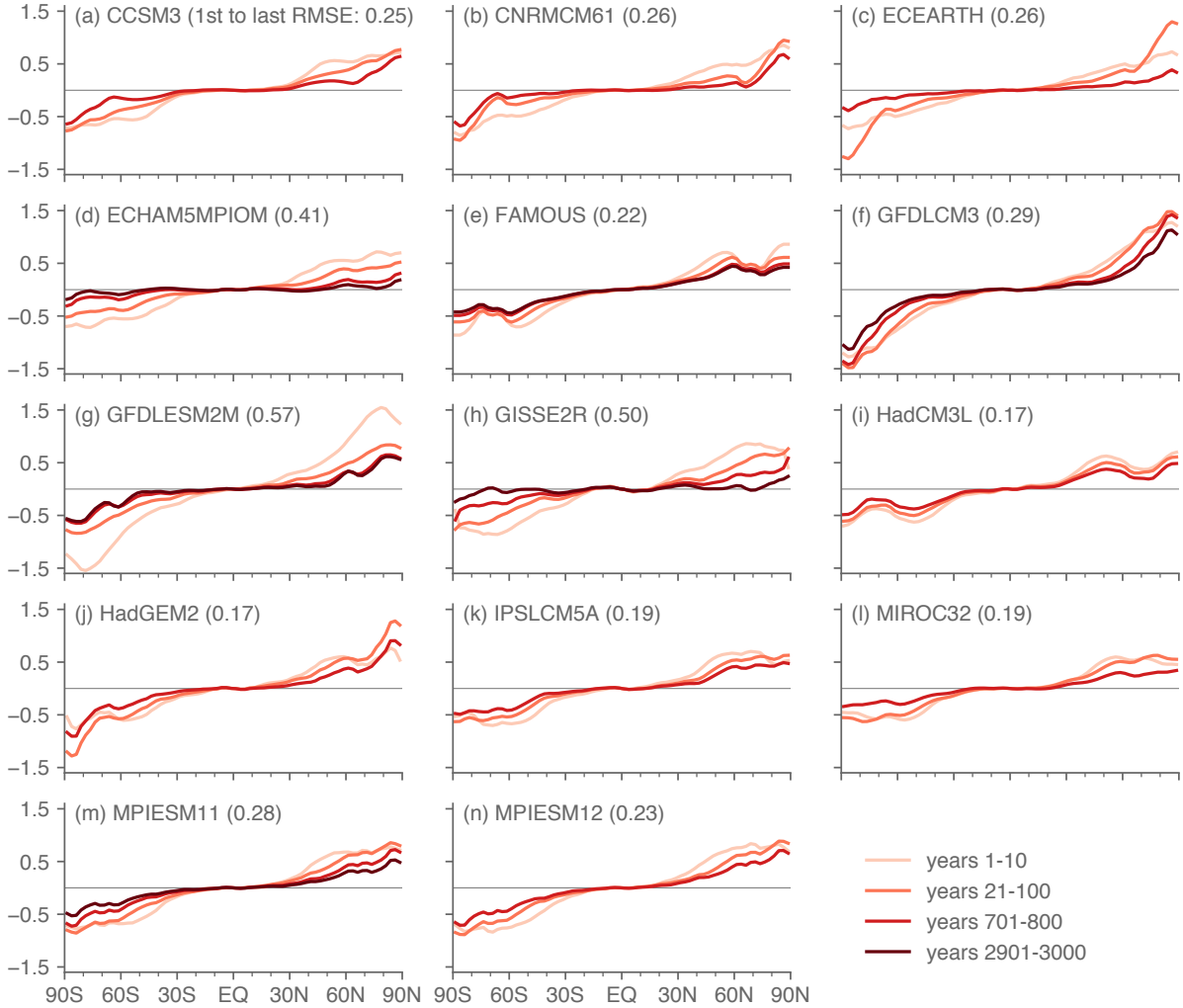


FIG. 3. As in Fig. 2 but for the hemispherically antisymmetric component. Note that the vertical axis range differs from Fig. 2 but has the same spacing.

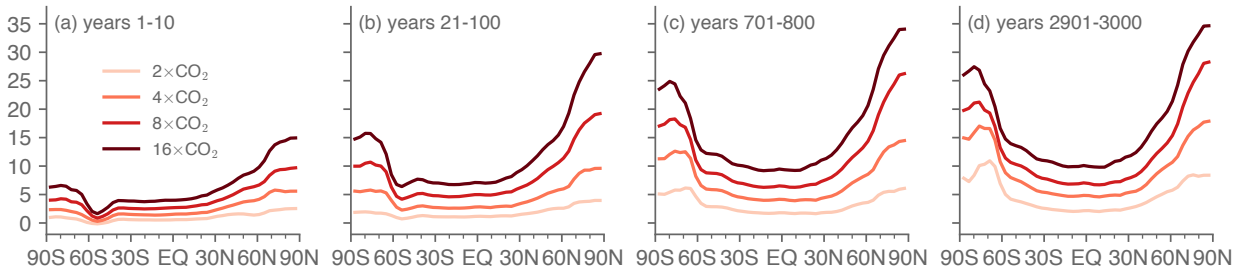


FIG. 4. Annual-mean, zonal-mean surface air temperature response in the 2, 4, 8, and 16 \times CO₂ simulations averaged over years (a) 1-10, (b) 21-100, (c) 701-800, and (d) 2901-3000.

also changes weakly (which is weaker overall than nearly all CO₂ cases). In short, the persistence of a symmetric warming signal that emerges in early decades is not unique

to quasi-uniform, longwave radiative forcing, but emerges under highly meridionally structured (though still largely hemispherically symmetric), shortwave forcing.

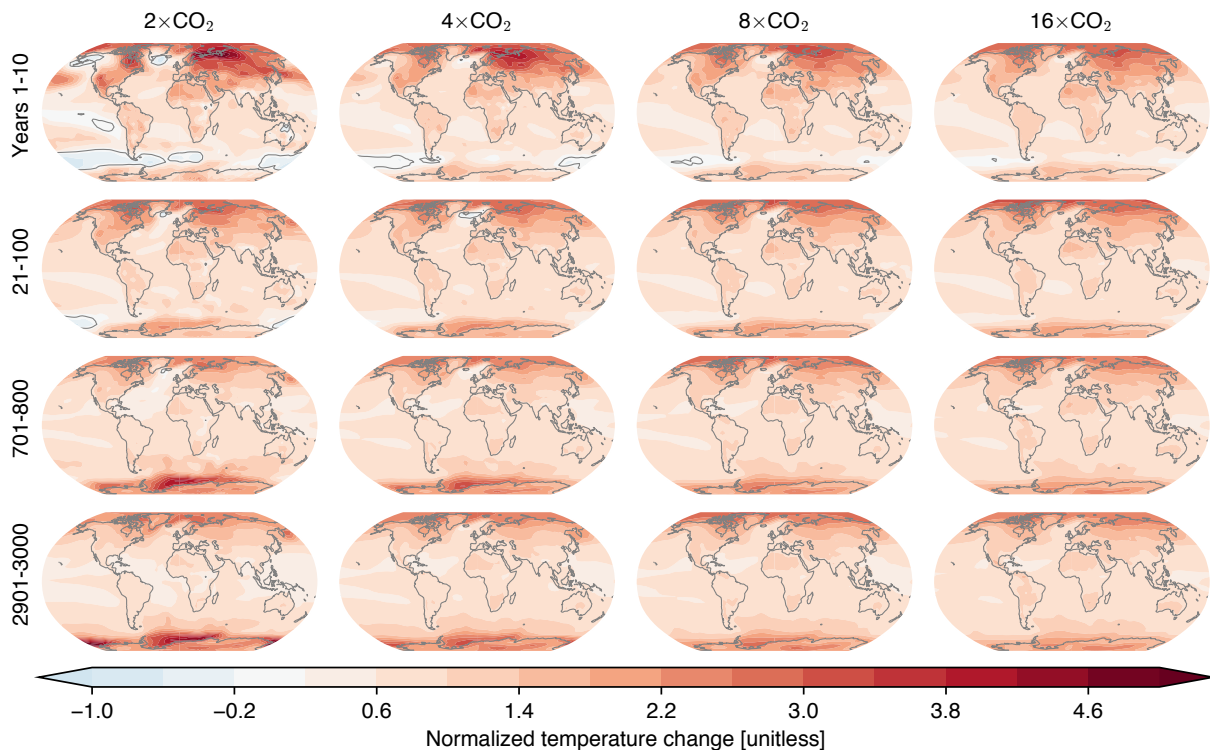


FIG. 5. Global-mean-normalized, annual-mean surface air temperature response in the 2, 4, 8, and 16 \times CO₂ GCM simulations according to the colorbar, each shown separately for each of the four time periods, as indicated by the column and row labels. The zero contour is shown as a thin gray contour.

5. Moist Energy Balance Model

Fig. 8 shows the surface air temperature response at each time period in the CESM 4 \times CO₂ simulation and the corresponding MEBM simulations; recall that across the MEBM simulations the only difference is the time period of the GCM from which λ and \mathcal{O} are taken. The MEBM captures the global-mean warming and raw warming patterns reasonably well (panel a) and therefore the mean-normalized patterns (panel b). The most prominent biases are insufficiently sharp warming gradients at high latitudes, particularly in the Southern Hemisphere (a common feature of MEBMs with a uniform diffusivity, e.g. Bonan et al. 2018), and this weaker gradient in the MEBM projects onto the hemispherically symmetric and antisymmetric (panels c and d) components of the mean-normalized warming pattern. Nonetheless, the MEBM captures the leading-order persistence of the initial symmetric pattern and the next-order increasing polar amplification with time. It also largely captures the salient features of the antisymmetric component, though in the latter two time periods with excessive Antarctic relative to Arctic warming.

We deem the correspondence between the MEBM and CESM simulations suitably accurate to justify using the

MEBM to further probe the underlying physical mechanisms. Specifically, we have performed additional simulations in which the antisymmetric components of the radiative feedback parameter and ocean heat uptake are artificially enhanced or suppressed. Using the radiative feedback parameter, for example, we have $\lambda^* = \lambda_{\text{sym}} + \alpha\lambda_{\text{asym}}$, where λ^* is the modified feedback parameter, λ_{sym} and λ_{asym} are the unmodified symmetric and antisymmetric components of the original feedback parameter λ , and α is a multiplicative factor ranging from 0 to 4.

Fig. 9 shows the mean-normalized full, symmetric, and antisymmetric warming patterns for each of the four time periods with α set to either 0, 1 (i.e. no modification), or 3 (results are similar for α values up to ~ 4 , above which the simulations begin behaving erratically; not shown). The full pattern (panel a) and antisymmetric components (panel c) are strongly modified for each time period by α .¹ Nevertheless, partially excepting the first decade for the largest α value, the symmetric component (panel b) is weakly modified. The weakening of the antisymmetric

¹Modest antisymmetries in the $\alpha = 0$ case stem from the radiative forcing and the climatological surface air temperature used to compute $\partial_T q$; in additional simulations with these also symmetrized (not shown), the warming pattern is exactly symmetric and very similar to the $\alpha = 0$ symmetric pattern shown.

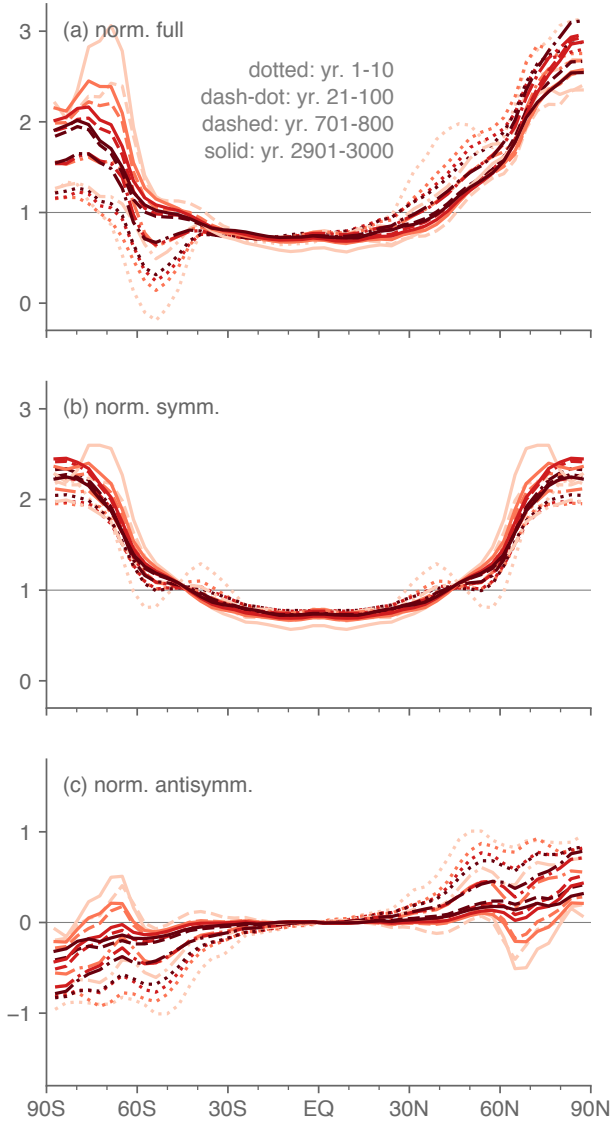


FIG. 6. Annual-mean, zonal-mean surface air temperature response in the 2, 4, 8, and 16 \times CO₂ according to the legend in Fig. 4 averaged within each of the four time periods of focus, with dotted, dash-dotted, dashed, and solid curves corresponding to years 1-10, 21-100, 701-800, and 2901-3000, respectively, normalized by the global-mean response for that forcing and time period. Shown are (a) the full field and the hemispherically (b) symmetric and (c) antisymmetric components. Note that the vertical axis range is identical in panels (a) and (b) but not in (c), while the vertical axis spacing is identical in all three panels.

component also remains in all cases, including for $\alpha \neq 0$ the eventual sign reversal.

These results suggest that the mean-normalized, symmetric warming component is governed primarily by hemispherically symmetric processes within the MEBM (otherwise, in principle covarying antisymmetric components of different terms could appreciably influence the

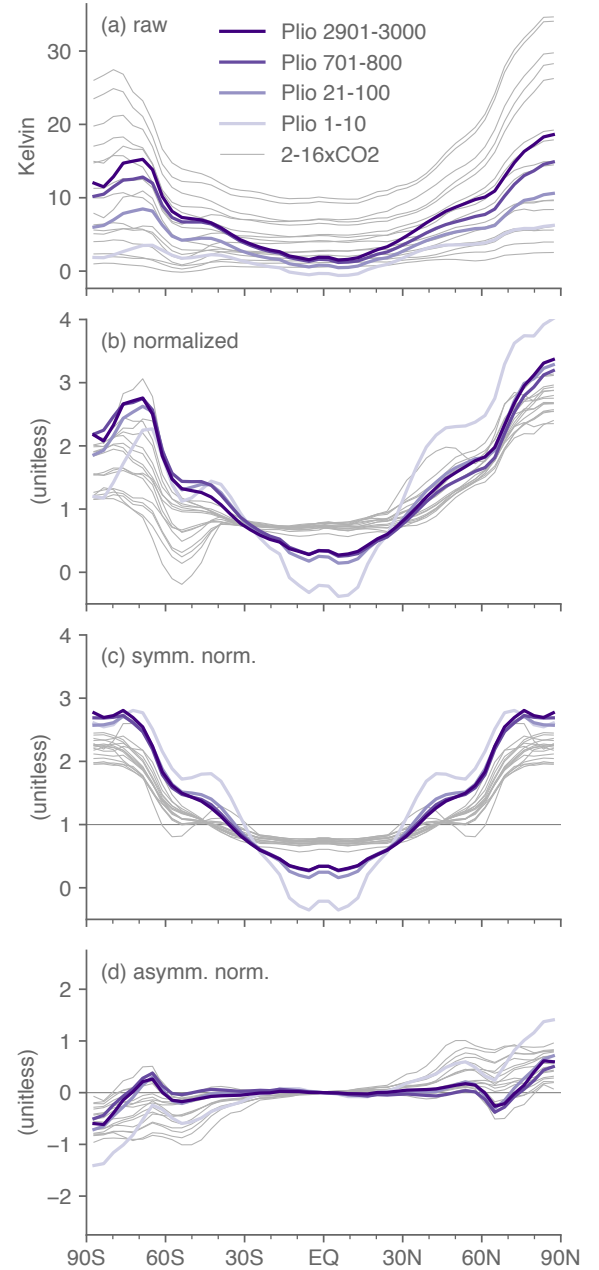


FIG. 7. Annual-mean, zonal-mean surface air temperature anomaly in the Pliocene simulation in each of the selected timescales and shown (a) raw, (b) normalized by its global mean, (c) the mean-normalized symmetric component, and (d) the mean-normalized antisymmetric component. Thin underlain curves are from the abrupt 2-16 \times CO₂ simulations for comparison.

hemispherically symmetric warming component). It remains to assess the behavior of the symmetric components of λ and \mathcal{O} , which are shown for each of the four time periods in Fig. 10 along with their full fields and antisym-

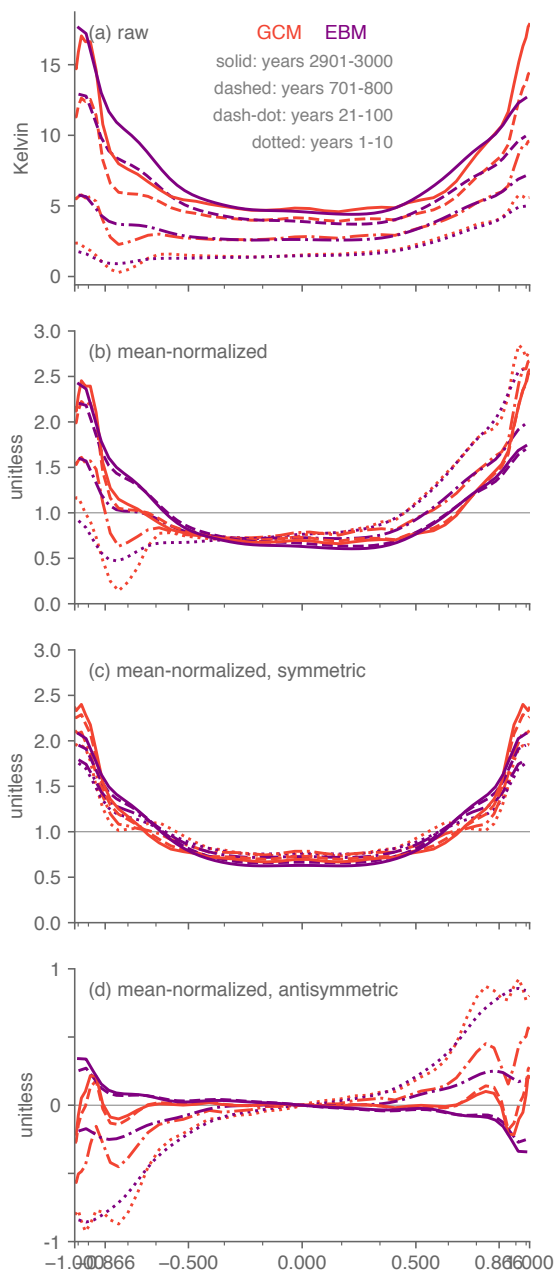


FIG. 8. Surface air temperature response in the GCM $4\times\text{CO}_2$ simulation at the four selected time periods and in the moist energy balance model simulations meant to reproduce the GCM $4\times\text{CO}_2$ simulation at each of those time periods, as indicated by the text in panel (a). Panels from top to bottom show the temperature (a) raw (in units Kelvin), (b) mean-normalized (unitless), (c) mean-normalized symmetric component (unitless), and (d) mean-normalized antisymmetric component (unitless). Note differing vertical axis spans in each panel.

metric components, as well as the radiative forcing which is constant in time.

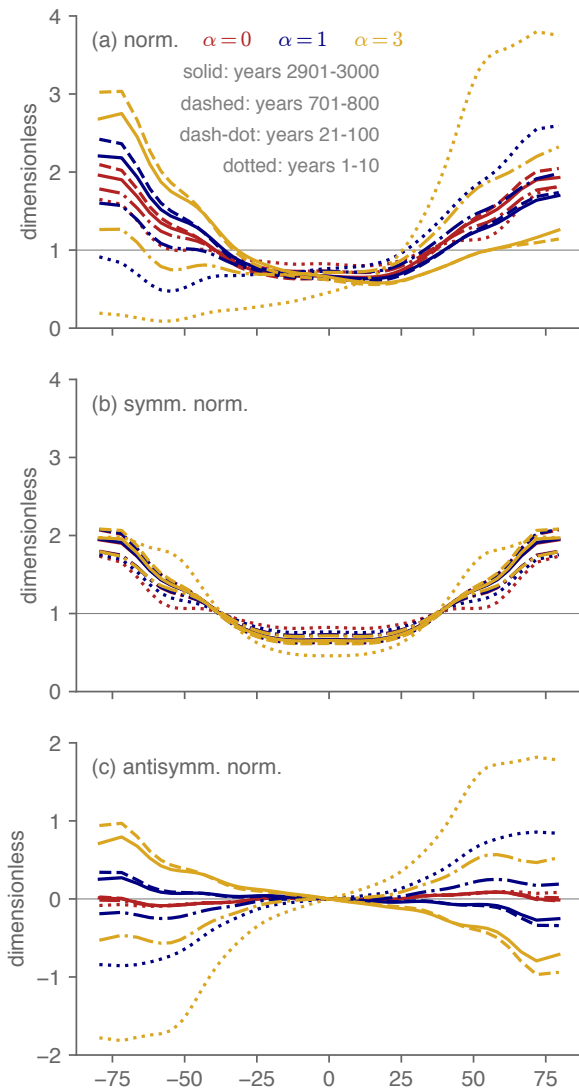


FIG. 9. Mean-normalized (a) full, (b) symmetric, and (c) antisymmetric surface air temperature anomaly fields in MEBM simulations with the antisymmetric components of the radiative feedback parameter and ocean heat uptake fields multiplied by the factor α , with red curves for $\alpha = 0$, blue for $\alpha = 1$ (i.e. unchanged), and dark yellow for $\alpha = 3$. Dotted, dash-dotted, dashed, and solid lines correspond to years 1-10, 21-100, 701-800, and 2901-3000 respectively of the CESM1.0.4 abrupt $4\times\text{CO}_2$ simulation. Note that the vertical axis range is identical in panels (a) and (b) but not (c), while the vertical axis spacing is identical in all three panels.

The radiative feedback parameter is negative at nearly all latitudes in all time periods, and generally more negative in the tropics than high latitudes (except in the first decade when the global minimum of approximately $-6 \text{ W m}^{-2} \text{ K}^{-1}$ occurs over the Southern Ocean). The symmetric component becomes less negative at most latitudes with time, which as is known results in climate sen-

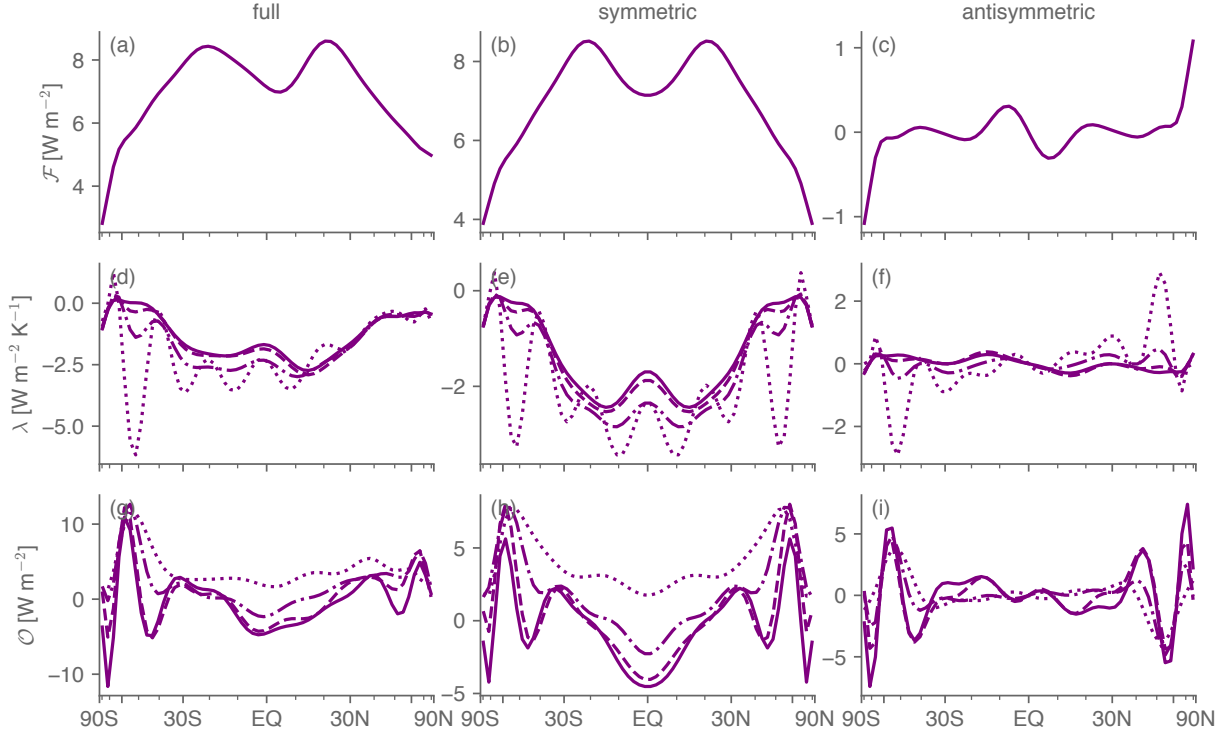


FIG. 10. From top to bottom, radiative forcing (\mathcal{F} , units W m^{-2}), radiative feedback parameter (λ , units $\text{W m}^{-2} \text{K}^{-1}$), and ocean heat uptake (\mathcal{O} , signed positive downward into the ocean, units W m^{-2}) fields used for the moist EBM simulations for each time period according to the text in panel c, with radiative forcing constant across time periods. From left to right, panels show the full fields, the hemispherically symmetric component, and the hemispherically antisymmetric component.

sitivity increasing with time (Armour et al. 2013). The global mean value of ocean heat uptake also varies, arguably more dramatically, from 3.9 W m^{-2} in the first decade to near zero at near-equilibrium. The symmetric component takes up heat from the atmosphere initially at all latitudes, but at low latitudes this weakens and ultimately changes sign. The bulk meridional slope from the most negative values in the deep tropics to the extratropics steepens with time. We speculate that these two properties of the ocean heat uptake response compensate as follows. As the global-mean \mathcal{O} decreases toward zero, the associated polar-amplified cooling reduces, also acting to increase the polar-amplified warming (S. Hu et al, “Global warming pattern formation: the role of ocean heat uptake”, submitted manuscript to *Journal of Climate*). But as the ocean heat uptake meridional slope increases, the low-latitude oceans flux comparatively more heat to the atmosphere and the high latitude oceans comparatively less, acting to counter polar amplification Rose et al. (2014).

6. Box model of amplification indices

We now distill the time evolution of Arctic, Antarctic, and lower-latitude surface warming into region averages and subsequently use a simple three-box, two-

timescale model to interpret the evolution of the symmetric and antisymmetric warming components (at the more granular level of these box averages rather than latitude-by-latitude). This amounts to an extension from the global mean to regional averages of the “fast” and “slow” timescale model of Held et al. (2010) and further developed and applied to CMIP5 GCMs by Geoffroy et al. (2013) (see also Geoffroy and Saint-Martin 2014).² In addition to CESM, we apply this analysis to FAMOUS from LongRunMIP, both for the abrupt4 $\times\text{CO}_2$ simulation. These two models illustrate the considerable model dependence in the behaviors of either polar cap, while the results for FAMOUS facilitate a useful though imperfect analytical approximation.

The two-timescale solution is given by

$$T(t) = T_{\text{eq}} \left[a_f \left(1 - e^{-t/\tau_f} \right) + a_s \left(1 - e^{-t/\tau_s} \right) \right], \quad (2)$$

²The box model is also analogous to that introduced by Armour et al. (2013) to characterize the time evolution of the effective climate sensitivity, with the boxes corresponding to land, low-latitude oceans, and high-latitude oceans. In effect, we reassign their land box to be the Arctic, their high-latitude ocean box to be the Antarctic, and their low-latitude ocean box to be our low-latitude (both land and ocean) box, and we assume a two-timescale rather than one-timescale warming evolution within each box.

where T_{eq} is the equilibrium temperature change, τ_f and τ_s are the fast and slow warming timescales, respectively, and a_f and a_s are weights such that $a_f + a_s = 1$. We fit the five parameters T_{eq} , a_f , a_s , τ_f , and τ_s for each region to the GCM results using annual-mean timeseries and nonlinear least-squares (as implemented in the “curve_fit” function of the scipy Python package).

Figure 11(a,b) shows the annual timeseries of the surface air temperature anomaly averaged over the Arctic (60–90°N), Antarctic (60–90°S), and lower-latitude (60°S–60°N) regions from the FAMOUS and CESM abrupt4×CO₂ simulations with a 10-year running mean applied. Equilibrium mean warming is much higher in FAMOUS than CESM in the Arctic and lower latitudes but not the Antarctic. CESM also exhibits considerable centennial-timescale variability particularly after ~1500 yr, roughly coinciding with the emergence of the Pacific Meridional Overturning Circulation detailed by Burls et al. (2017). Overlain for each region and model is the best-fit two timescale model. For FAMOUS the two-timescale fit captures the evolution rather well. The fit for CESM is poorer, with too sharp a shoulder after the initial decades especially for the Arctic and lower latitudes.

Table 2 lists the best fit parameters for each. For FAMOUS, the weight of the fast component for the equilibrium varies modestly across the regions, 66% for lower latitudes to 78% for the Arctic. The fast timescale differs by only ~12% across the three regions, from 14.1 years for lower latitudes to 15.9 for the Arctic. The slow timescale is comparable for the lower latitudes and Arctic (433 and 471 years respectively), but appreciably longer, 588 years for the Antarctic. Nevertheless, the ~26% difference in the slow timescales motivates us to consider, as the simplest approximation, the case where there is no difference in either timescale across the regions.

Let T_N be the Arctic cap temperature, T_S be the Antarctic cap temperature, and T_L be the low-latitude box temperature. We neglect ocean heat uptake and atmospheric energy transport perturbations, assume a time-invariant and spatially uniform radiative forcing R , and assume for each box a time-invariant radiative feedback parameter λ_i , such that each box’s equilibrium temperature anomaly is $T_{eq,i} \equiv -R/\lambda_i$. Nevertheless, we stress that the ocean heat uptake and atmospheric energy flux divergence fields implicitly influence the best-fit values of all five parameters to the GCM results.

The symmetric and antisymmetric warming components in this context are respectively $S \equiv (T_N + T_S)/2$ and $A \equiv (T_N - T_S)/2$. Letting γ be the ratio of the low-latitude surface area to the surface areas of either polar cap, then the global-mean temperature anomaly at any given time is $\bar{T} = (T_S + \gamma T_L + T_N)/(\gamma + 2)$; with our choice of region borders at 60°S/N, $\gamma \approx 6.5$.

Assuming each of τ_f , τ_s , a_f and a_s do not vary across the three boxes, the global-mean temperature anomaly is

$$\bar{T}(t) = \frac{T_{eq,S} + \gamma T_{eq,L} + T_{eq,N}}{\gamma + 2} \left[a_f (1 - e^{-t/\tau_f}) + a_s (1 - e^{-t/\tau_s}) \right]. \quad (3)$$

And the global-mean-normalized temperature anomaly in an individual box is

$$\frac{T_i(t)}{\bar{T}(t)} = \frac{(\gamma + 2)T_{eq,i}}{T_{eq,S} + \gamma T_{eq,L} + T_{eq,N}}, \quad i \in \{N, L, S\}. \quad (4)$$

This is independent of time. In addition, under uniform radiative forcing R , since $T_{eq,i} \equiv -R/\lambda_i$, it is also independent of the radiative forcing. Since the mean-normalized temperature change in each box is independent of time, so too are the symmetric and antisymmetric components of the mean-normalized warming pattern. The time- and forcing-independence of the mean-normalized symmetric component capture the leading order behavior but not (for most GCMs) the slight increase in polar amplification with time, and the time-independence of the antisymmetric component is at odds with its (for most GCMs) gradual weakening with time.

Fig. 11(c) shows the mean-normalized Arctic, Antarctic, and lower-latitude temperature anomaly timeseries for FAMOUS along with the prediction for each under this uniform timescales approximation. The box model underestimates the warming in each case, but nevertheless the GCM timeseries vary weakly in time, at most for the Arctic by ~10% over the 3,000 years.

The results from CESM are less amenable to a clean analytical approximate solution. The Arctic v. Antarctic equilibrium warming values are similar (with slightly more Antarctic warming as noted above), both roughly three times that of the lower latitudes. This also holds for the slow timescale, which is roughly twice the lower-latitude value in either polar cap. Conversely, the fast timescale is comparable in the Arctic and lower-latitude boxes but several times longer for the Antarctic. The relative weights of the fast vs. short timescales are fairly even in all three boxes.

Despite the approximations made for FAMOUS being poorly justified for CESM rather than FAMOUS, we show in Fig. 11(d) the mean-normalized Arctic, Antarctic, and lower-latitude temperature anomaly timeseries from the CESM abrupt 4×CO₂ simulation along with the prediction for each under the uniform timescales approximation. The predicted time-invariance for each region is reasonable for the lower latitudes but quite poor for the polar caps, the Antarctic especially. Nevertheless, values near the end of the simulation lie reasonably close to the analytical approximation.

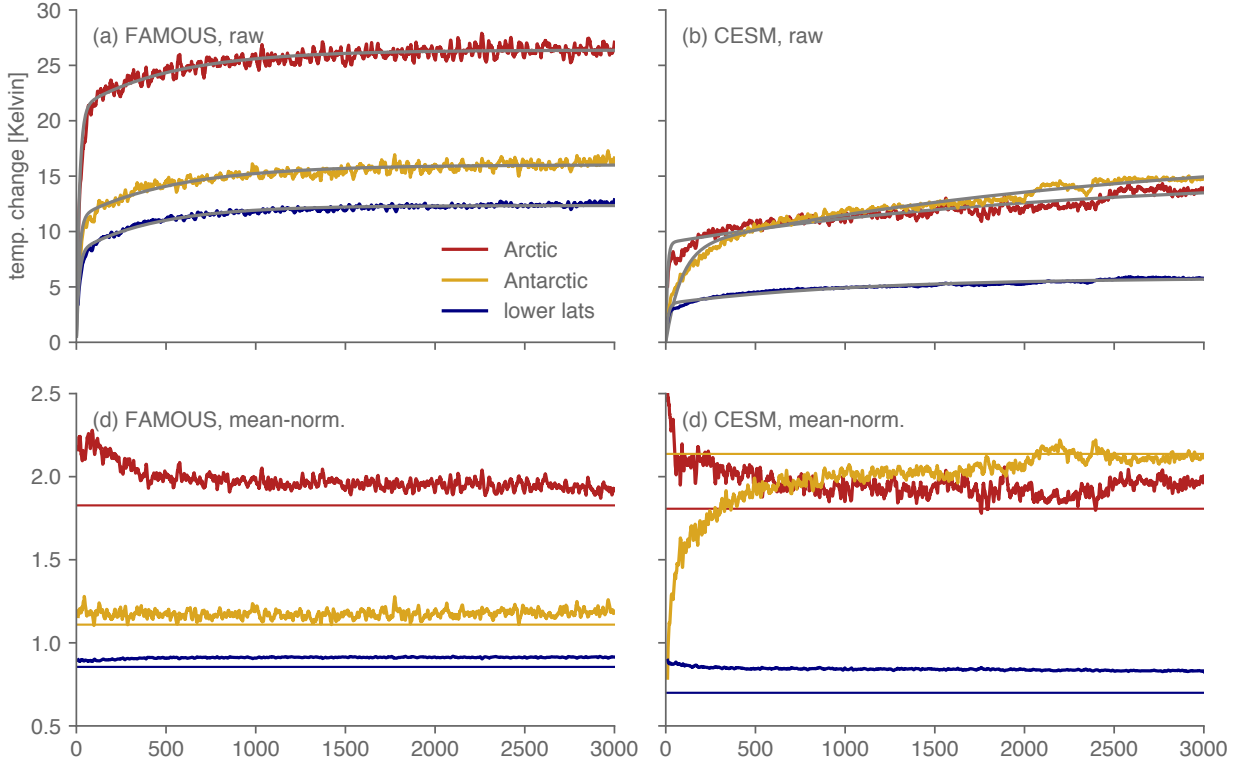


FIG. 11. Timeseries of 10-year running mean of (red) Arctic, (yellow) Antarctic, and (blue) low-latitude box-average temperatures in the abrupt $4\times\text{CO}_2$ simulation in (left) FAMOUS and (right) CESM. Overlain gray curves are the fits from the simple two-layer box model for each region. The top row shows raw fields, and the bottom row shows the same timeseries but each normalized by the global-mean warming, along with thinner horizontal lines indicating the predictions from the box model under the approximation of horizontally uniform fast and slow warming timescales, as described in the text.

	CESM					FAMOUS				
	T_{eq} [K]	τ_f [yr]	a_f	τ_s [yr]	a_s	T_{eq} [K]	τ_f [yr]	a_f	τ_s [yr]	a_s
Arctic	15.1	9.4	0.59	2223	0.41	26.4	15.9	0.78	471	0.22
Antarctic	17.8	85.3	0.48	2564	0.52	16.1	15.3	0.71	588	0.29
Lower lats	5.8	12.7	0.60	1065	0.40	12.3	14.1	0.66	433	0.34
Globe	7.1	15.9	0.58	1188	0.42	13.5	14.5	0.68	445	0.32

TABLE 2. Best-fit values of the five parameters in the two-timescale model for the abrupt $4\times\text{CO}_2$ simulations in CESM1.0.4 and in FAMOUS for each of the three regions of our box model and for the global mean. Units are Kelvin for T_{eq} and years for τ_f and τ_s ; a_f and a_s are dimensionless.

7. Conclusions

We decompose the zonal-mean surface air temperature response to increased CO_2 from decadal to millennial timescales into hemispherically symmetric and antisymmetric components for fourteen models from LongRunMIP and in a low-resolution version of the CESM1.0.4 GCM. In all models, to leading order the hemispherically symmetric component, normalized by the global-mean, varies weakly from the first decade to (near) equilibrium. And in ten of the fifteen total models analyzed, though the symmetric normalized warming is fixed to first order, to

second order it tends to evolve toward higher polar amplification with time. Thus, the polar amplification that it exhibits in earlier periods can be thought of roughly as a lower bound on the subsequent polar amplification. It also varies weakly across CO_2 magnitudes from $2\text{--}16\times$ in CESM1 and across timescales in a simulation generating an early Pliocene-like surface climate attained through meridionally patterned cloud albedo perturbations. Thus, the symmetric component is insensitive in time and to forcing magnitude for a given forcing structure, but unsurprisingly its shape depends on the forcing structure.

A simple moist energy balance model prescribed with ocean heat uptake and radiative feedback fields inferred from four different time periods of the $4\times\text{CO}_2$ GCM simulation captures the GCM zonal-mean warming pattern well overall. Additional simulations in the MEBM in which the antisymmetric components of the radiative feedback parameter and ocean heat uptake fields are artificially weakened or enhanced generally yield mean-normalized symmetric warming patterns quite similar to that of the full simulations, suggesting a weak role for any rectifying interactions among antisymmetric components of any fields onto the symmetric component of surface warming. The ocean heat uptake decreases with time toward zero at equilibrium in the global average, and its meridional slope steepens, changes that likely compensate with respect to the amount of polar amplification, thereby establishing the persistence of the symmetric warming pattern.

A simple three-box, two-timescale model of warming in the Arctic, Antarctic, and lower-latitude sectors was fit to 3,000-yr timeseries of annual-mean surface warming in the CESM1.0.4 and FAMOUS abrupt $4\times\text{CO}_2$ simulations. In FAMOUS, the fast and slow timescales of each region are such that a reasonable analytical approximation can be attained that yields time-invariance of both the symmetric and antisymmetric mean-normalized warming patterns in terms of these box averages. In CESM1.0.4, the behavior is more complicated and the approximations underlying the analytical solution are less justified.

That the mean-normalized symmetric warming component in the MEBM is weakly modified even when the antisymmetric terms are strongly amplified helps explain the robustness of the result across the GCMs: if its behavior depended sensitively on the relative magnitudes of the symmetric and antisymmetric components of λ and \mathcal{O} —which surely varies appreciably across GCMs—then the behaviors would be less robust.

It would be interesting to investigate relationships in the LongRunMIP models among these behaviors with other properties of their CO_2 -forced climates. Questions include: are there appreciable correlations between these properties of the symmetric and antisymmetric components on the one hand with e.g. climate sensitivity? What is the primary source of the differences among models in the symmetric component? What determines the amount of antisymmetry in the equilibrium pattern?

APPENDIX A

Moist energy balance model formulation

For the CO_2 radiative forcing, $\mathcal{F}(\varphi)$, we use the spatially varying instantaneous forcing of Huang et al. (2016) computed for a doubling of CO_2 . This will not be identical to the radiative forcing computed with our particular GCM due to dependencies on the climatology (e.g. Merlis

2015; Huang et al. 2017). But we do not expect such discrepancies to meaningfully impact the results. In order to convert this instantaneous $2\times\text{CO}_2$ radiative forcing field into a stratosphere-adjusted $4\times\text{CO}_2$ radiative forcing, we double it and add a uniform value of 2.4 W m^{-2} . This yields a global-mean value of 7.0 W m^{-2} .

The feedback parameter λ is diagnosed using this radiative forcing field along with fields taken from the GCM $4\times\text{CO}_2$ simulation:

$$\lambda(\varphi) = -\frac{\mathcal{F}(\varphi) - \mathcal{T}(\varphi)}{T_{\text{gcm}}(\varphi)}, \quad (\text{A1})$$

where \mathcal{T} is the anomalous TOA radiative flux in the GCM (signed positive downward), and T_{gcm} is the anomalous surface air temperature in the GCM. The “gcm” subscript is meant to emphasize that the temperature field in the denominator of (A1) is that diagnosed from the GCM, not the MEBM’s own computed temperature (whereas the temperature field that λ multiplies in (1) is that of the MEBM). Thus, all terms on the RHS, and therefore the resulting λ fields, are diagnosed from the GCM. One MEBM simulation is performed for each of the four time periods of interest, each with \mathcal{T} and T_{gcm} taken from the GCM $4\times\text{CO}_2$ simulation averaged over that time period. Likewise, the prescribed ocean heat uptake field \mathcal{O} is simply diagnosed from the $4\times\text{CO}_2$ GCM simulation for the given time period.

For the diffusive approximation to atmospheric energy transport convergence, because all quantities are anomalies, surface MSE is linearized as $h = T(1 + \mathcal{H}L\partial_T q^*)/c_p$, with relative humidity \mathcal{H} , saturation specific humidity q^* , and latent heat of vaporization L . The partial derivative of the saturation vapor pressure, $\partial_T q^*$, is evaluated using the zonal-mean climatological surface air temperature from the GCM averaged over years 701–800 of the control simulation. The parameter values for all constant coefficients are standard: $\mathcal{H} = 0.8$, $\mathcal{D} = 0.3 \text{ W m}^{-2} \text{ K}^{-1}$, $c_p = 1004.6 \text{ J kg}^{-1} \text{ K}^{-1}$, and $L = 2.5 \times 10^6 \text{ J kg}^{-1}$.

The MEBM is integrated in time using a fourth-order Runge-Kutta scheme to equilibrium, while a second-order finite difference scheme is used for the ∇^2 operator (Wagner and Eisenman 2015). There are 60 model grid points evenly spaced in $\sin \varphi = 1/30$ increments, with gridpoint centers in each hemisphere from $\sin \varphi \approx 0.12$ (corresponding to $\varphi \approx 4.8^\circ$) to $\sin \varphi \approx 0.98$ (corresponding to $\varphi \approx 79.5^\circ$). The GCM fields are spaced evenly in latitude, with 48 points total, spanning in each hemisphere from approximately 1.8 to 87.2° with approximately 3.6° spacing. The GCM fields used as inputs to the MEBM are spectrally transformed at order 20 to the MEBM grid.

Acknowledgments. We thank William Wang for generating several figures that facilitated our analyses. S.A.H. was supported during different periods of this study by

an NSF Atmospheric and Geospace Sciences Postdoctoral Research Fellowship (NSF Award #1624740), a Caltech Foster and Coco Stanback Postdoctoral Fellowship, and a Columbia University Earth Institute Fellowship. T.M.M. acknowledges support from NSERC. N.J.B. acknowledges support from NSF Award #1844380 and is supported by the Alfred P. Sloan Foundation as a Research Fellow. Three anonymous reviewers provided extremely useful comments and motivated the analyses of LongRunMIP and the simple box model.

References

- Andrews, T., J. M. Gregory, and M. J. Webb, 2015: The Dependence of Radiative Forcing and Feedback on Evolving Patterns of Surface Temperature Change in Climate Models. *J. Climate*, **28** (4), 1630–1648, doi:10.1175/JCLI-D-14-00545.1.
- Armour, K. C., C. M. Bitz, and G. H. Roe, 2013: Time-Varying Climate Sensitivity from Regional Feedbacks. *J. Climate*, **26** (13), 4518–4534, doi:10.1175/JCLI-D-12-00544.1.
- Armour, K. C., N. Siler, A. Donohoe, and G. H. Roe, 2019: Meridional Atmospheric Heat Transport Constrained by Energetics and Mediated by Large-Scale Diffusion. *J. Climate*, **32** (12), 3655–3680, doi:10.1175/JCLI-D-18-0563.1.
- Bonan, D. B., K. C. Armour, G. H. Roe, N. Siler, and N. Feldl, 2018: Sources of Uncertainty in the Meridional Pattern of Climate Change. *Geophys. Res. Lett.*, **45** (17), 9131–9140, doi:10.1029/2018GL079429.
- Burls, N. J., and A. V. Fedorov, 2014a: Simulating Pliocene warmth and a permanent El Niño-like state: The role of cloud albedo. *Paleoceanography*, **29** (10), 893–910, doi:10.1002/2014PA002644.
- Burls, N. J., and A. V. Fedorov, 2014b: What Controls the Mean East–West Sea Surface Temperature Gradient in the Equatorial Pacific: The Role of Cloud Albedo. *J. Climate*, **27** (7), 2757–2778, doi:10.1175/JCLI-D-13-00255.1.
- Burls, N. J., A. V. Fedorov, D. M. Sigman, S. L. Jaccard, R. Tiedemann, and G. H. Haug, 2017: Active Pacific meridional overturning circulation (PMOC) during the warm Pliocene. *Science Advances*, **3** (9), e1700156, doi:10.1126/sciadv.1700156.
- Danabasoglu, G., and P. R. Gent, 2009: Equilibrium Climate Sensitivity: Is It Accurate to Use a Slab Ocean Model? *J. Climate*, **22** (9), 2494–2499, doi:10.1175/2008JCLI2596.1.
- Dong, Y., K. C. Armour, M. D. Zelinka, C. Proistosescu, D. S. Battisti, C. Zhou, and T. Andrews, 2020: Intermodel Spread in the Pattern Effect and Its Contribution to Climate Sensitivity in CMIP5 and CMIP6 Models. *Journal of Climate*, **33** (18), 7755–7775, doi:10.1175/JCLI-D-19-1011.1.
- Fedorov, A. V., N. J. Burls, K. T. Lawrence, and L. C. Peterson, 2015: Tightly linked zonal and meridional sea surface temperature gradients over the past five million years. *Nature Geosci.*, **8** (12), 975–980, doi:10.1038/ngeo2577.
- Feldl, N., B. T. Anderson, and S. Bordoni, 2017: Atmospheric Eddies Mediate Lapse Rate Feedback and Arctic Amplification. *J. Climate*, **30** (22), 9213–9224, doi:10.1175/JCLI-D-16-0706.1.
- Flannery, B. P., 1984: Energy Balance Models Incorporating Transport of Thermal and Latent Energy. *J. Atmos. Sci.*, **41** (3), 414–421, doi:10.1175/1520-0469(1984)041<0414:EBMITO>2.0.CO;2.
- Geoffroy, O., and D. Saint-Martin, 2014: Pattern decomposition of the transient climate response. *Tellus A: Dynamic Meteorology and Oceanography*, **66** (1), 233–239, doi:10.3402/tellusa.v66.23393.
- Geoffroy, O., D. Saint-Martin, D. J. L. Olivé, A. Voldoire, G. Bellon, and S. Tytéc, 2013: Transient Climate Response in a Two-Layer Energy-Balance Model. Part I: Analytical Solution and Parameter Calibration Using CMIP5 AOGCM Experiments. *Journal of Climate*, **26** (6), 1841–1857, doi:10.1175/JCLI-D-12-00195.1.
- Heede, U. K., A. V. Fedorov, and N. J. Burls, 2020: Time Scales and Mechanisms for the Tropical Pacific Response to Global Warming: A Tug of War between the Ocean Thermostat and Weaker Walker. *Journal of Climate*, **33** (14), 6101–6118, doi:10.1175/JCLI-D-19-0690.1.
- Held, I. M., M. Winton, K. Takahashi, T. Delworth, F. Zeng, and G. K. Vallis, 2010: Probing the Fast and Slow Components of Global Warming by Returning Abruptly to Preindustrial Forcing. *Journal of Climate*, **23** (9), 2418–2427, doi:10.1175/2009JCLI3466.1.
- Henry, M., T. M. Merlis, N. J. Lutsko, and B. E. J. Rose, 2021: Decomposing the Drivers of Polar Amplification with a Single-Column Model. *Journal of Climate*, **34** (6), 2355–2365, doi:10.1175/JCLI-D-20-0178.1.
- Huang, Y., X. Tan, and Y. Xia, 2016: Inhomogeneous radiative forcing of homogeneous greenhouse gases. *Journal of Geophysical Research: Atmospheres*, **121** (6), 2780–2789, doi:10.1002/2015JD024569.
- Huang, Y., Y. Xia, and X. Tan, 2017: On the pattern of CO₂ radiative forcing and poleward energy transport. *J. Geophys. Res. Atmos.*, **122** (20), 2017JD027221, doi:10.1002/2017JD027221.
- Hwang, Y.-T., D. M. W. Frierson, and J. E. Kay, 2011: Coupling between Arctic feedbacks and changes in poleward energy transport. *Geophysical Research Letters*, **38** (17), doi:10.1029/2011GL048546.
- Jansen, M. F., L.-P. Nadeau, and T. M. Merlis, 2018: Transient versus Equilibrium Response of the Ocean's Overturning Circulation to Warming. *J. Climate*, **31** (13), 5147–5163, doi:10.1175/JCLI-D-17-0797.1.
- Krinner, G., and M. G. Flanner, 2018: Striking stationarity of large-scale climate model bias patterns under strong climate change. *PNAS*, **115** (38), 9462–9466, doi:10.1073/pnas.1807912115.
- Li, C., J.-S. von Storch, and J. Marotzke, 2013: Deep-ocean heat uptake and equilibrium climate response. *Clim Dyn.*, **40** (5), 1071–1086, doi:10.1007/s00382-012-1350-z.
- Marshall, J., J. R. Scott, K. C. Armour, J.-M. Campin, M. Kelley, and A. Romanou, 2015: The ocean's role in the transient response of climate to abrupt greenhouse gas forcing. *Clim Dyn.*, **44** (7–8), 2287–2299, doi:10.1007/s00382-014-2308-0.
- Merlis, T. M., 2015: Direct weakening of tropical circulations from masked CO₂ radiative forcing. *PNAS*, **112** (43), 13 167–13 171, doi:10.1073/pnas.1508268112.
- Merlis, T. M., and M. Henry, 2018: Simple Estimates of Polar Amplification in Moist Diffusive Energy Balance Models. *J. Climate*, **31** (15), 5811–5824, doi:10.1175/JCLI-D-17-0578.1.

- Previdi, M., T. P. Janoski, G. Chiodo, K. L. Smith, and L. M. Polvani, 2020: Arctic Amplification: A Rapid Response to Radiative Forcing. *Geophysical Research Letters*, **n/a** (n/a), e2020GL089933, doi:10.1029/2020GL089933.
- Roe, G. H., N. Feldl, K. C. Armour, Y.-T. Hwang, and D. M. W. Frierson, 2015: The remote impacts of climate feedbacks on regional climate predictability. *Nature Geosci.*, **8** (2), 135–139, doi:10.1038/ngeo2346.
- Rose, B. E. J., K. C. Armour, D. S. Battisti, N. Feldl, and D. D. B. Koll, 2014: The dependence of transient climate sensitivity and radiative feedbacks on the spatial pattern of ocean heat uptake. *Geophysical Research Letters*, **41** (3), 1071–1078, doi:10.1002/2013GL058955.
- Rugenstein, M., and Coauthors, 2019: LongRunMIP: Motivation and Design for a Large Collection of Millennial-Length AOGCM Simulations. *Bull. Amer. Meteor. Soc.*, **100** (12), 2551–2570, doi:10.1175/BAMS-D-19-0068.1.
- Rugenstein, M., and Coauthors, 2020: Equilibrium Climate Sensitivity Estimated by Equilibrating Climate Models. *Geophysical Research Letters*, **47** (4), e2019GL083898, doi:10.1029/2019GL083898.
- Russotto, R. D., and M. Biasutti, 2020: Polar amplification as an inherent response of a circulating atmosphere: Results from the TRACMIP aquaplanets. *Geophysical Research Letters*, **n/a** (n/a), e2019GL086771, doi:10.1029/2019GL086771.
- Senior, C. A., and J. F. B. Mitchell, 2000: The time-dependence of climate sensitivity. *Geophysical Research Letters*, **27** (17), 2685–2688, doi:10.1029/2000GL011373.
- Shields, C. A., D. A. Bailey, G. Danabasoglu, M. Jochum, J. T. Kiehl, S. Levis, and S. Park, 2012: The Low-Resolution CCSM4. *J. Climate*, **25** (12), 3993–4014, doi:10.1175/JCLI-D-11-00260.1.
- Stephens, G. L., D. O'Brien, P. J. Webster, P. Pilewski, S. Kato, and J.-I. Li, 2015: The albedo of Earth. *Rev. Geophys.*, **53** (1), 2014RG000449, doi:10.1002/2014RG000449.
- Stuecker, M. F., and Coauthors, 2018: Polar amplification dominated by local forcing and feedbacks. *Nature Climate Change*, **8** (12), 1076, doi:10.1038/s41558-018-0339-y.
- Tebaldi, C., and J. M. Arblaster, 2014: Pattern scaling: Its strengths and limitations, and an update on the latest model simulations. *Climatic Change*, **122** (3), 459–471, doi:10.1007/s10584-013-1032-9.
- Voigt, A., B. Stevens, J. Bader, and T. Mauritsen, 2013: The Observed Hemispheric Symmetry in Reflected Shortwave Irradiance. *J. Climate*, **26** (2), 468–477, doi:10.1175/JCLI-D-12-00132.1.
- Voigt, A., B. Stevens, J. Bader, and T. Mauritsen, 2014: Compensation of Hemispheric Albedo Asymmetries by Shifts of the ITCZ and Tropical Clouds. *Journal of Climate*, **27** (3), 1029–1045, doi:10.1175/JCLI-D-13-00205.1.
- Wagner, T. J. W., and I. Eisenman, 2015: How Climate Model Complexity Influences Sea Ice Stability. *J. Climate*, **28** (10), 3998–4014, doi:10.1175/JCLI-D-14-00654.1.